Fluctuation-induced shear flow and energy transfer in plasma interchange turbulence

Citation: Li, B. et al. "Fluctuation-Induced Shear Flow and Energy Transfer in Plasma Interchange Turbulence." Physics of Plasmas 22, 11 (November 2015): 112304 © 2015 AIP Publishing LLC

As Published: http://dx.doi.org/10.1063/1.4935912

Publisher: American Institute of Physics (AIP)

Persistent URL: http://hdl.handle.net/1721.1/113245

Version: Author's final manuscript: final author's manuscript post peer review, without publisher's formatting or copy editing

Fluctuation-induced shear flow and energy transfer in plasma interchange turbulence

B. Li,[1,2] C. K. Sun,[1] X. Y. Wang,[1] A. Zhou,[1] X. G. Wang,[1] and D. R. Ernst[2]

[1]*School of Physics, State Key Laboratory of Nuclear Physics and Technology, Peking University, Beijing 100871, China*

[2]*Plasma Science and Fusion Center, Massachusetts Institute of Technology, Cambridge, Massachusetts 02139, USA*

(Dated: October 23, 2015)

Abstract

Fluctuation-induced $\boldsymbol{E}\times\boldsymbol{B}$ shear flow and energy transfer for plasma interchange turbulence are examined in a flux-driven system with both closed and open magnetic field lines. The nonlinear evolution of interchange turbulence shows the presence of two confinement regimes characterized by low and high $\boldsymbol{E}\times\boldsymbol{B}$ flow shear. In the first regime, the large-scale turbulent convection is dominant and the mean $\boldsymbol{E}\times\boldsymbol{B}$ shear flow is at a relatively low level. By increasing the heat flux above a certain threshold, the increased turbulent intensity gives rise to the transfer of energy from fluctuations to mean $\boldsymbol{E}\times\boldsymbol{B}$ flows. As a result, a transition to the second regime occurs, in which a strong mean $\boldsymbol{E}\times\boldsymbol{B}$ shear flow is generated.

PACS numbers: 52.35.Ra, 52.25.Fi, 52.25.Gj

I. INTRODUCTION

Turbulent transport and shear flows in the edge region of magnetically confined plasmas has been of long-standing interest to the plasma turbulence and fusion communities [1–25]. In particular, the turbulence-driven shear flow near the plasma edge triggered by increasing heating power is believed to play an important role in the formation of plasma edge transport barrier and the resulting higher global energy confinement [1–4]. The turbulent energy transfer has been proposed as a mechanism for the generation of mean shear flows. Many of the conceptual points concerning turbulent energy transfer have been studied in both reduced models and in experimental investigations [19–24]. The transfer of energy between fluctuations and sheared flows has also been demonstrated by fluid simulations for interchange turbulence with cold ions [10–12]. Recently, the formation of transport barrier has been simulated with fluid models [17–19], in which the neoclassical terms are added in the vorticity equation with cold ions. In these simulations [17–19], the mean shear flows are generated mainly due to the neoclassical terms. In the present hot-ion model [3, 4, 6–8], we consider the ion diamagnetic term in the vorticity with no additional neoclassical terms included in the vorticity equation. In the present simulation, the mean $\boldsymbol{E}\times\boldsymbol{B}$ shear flows are generated through the energy transfer induced by enhanced fluctuations. Both the previous and present fluid simulations show that the generation of mean $\boldsymbol{E}\times\boldsymbol{B}$ shear flow leads to the transport barrier formation.

In this work, we present self-consistent fluid simulations of the fluctuation-induced $\boldsymbol{E}\times\boldsymbol{B}$ shear flow and energy transfer for interchange turbulence in a flux-driven system with the geometry and parameters relevant to the edge region of magnetically confined plasmas. Our flux-driven, nonlinear simulations show that a great increase in the mean $\boldsymbol{E}\times\boldsymbol{B}$ flow and shear can be induced in a toroidal plasma by increasing the heat flux above a certain threshold. The model geometry comprises both closed and open field line regions, corresponding to the edge and scrape off layer (SOL) of magnetically confined fusion devices such as tokamaks. Thus the system provides a simplified setting in which to explore the basic physics of turbulent transport and shear flows in the edge region of tokamaks and similar devices. We focus on the interchange instability which is driven by the pressure gradients and magnetic curvature. For the interchange mode with the parallel wave number $k_{||} \simeq 0$ in the main plasma, the field-line-averaged two-dimensional (2D) model is used in this work. The closed

and open field line regions are distinguished by the parallel boundary conditions, and the last closed flux surface (LCFS) separates the two regions. At the end of open field lines, the sheath boundary conditions are imposed with the parallel flow $\boldsymbol{v}_{||i} = \pm c_s$ and parallel current $j_{||} = \pm enc_s[1 - \exp(3 - e\phi/T_e)]$ where $c_s = \sqrt{T_e/m_i}$ is the sound speed. This gives rise to the parallel losses in the open field line region and produces the pressure gradients near the LCFS, which drive interchange instability in the system. The nonlinear evolution of interchange turbulence shows the presence of two confinement regimes characterized by low and high $\boldsymbol{E} \times \boldsymbol{B}$ flow shear. In the first regime, the mean $\boldsymbol{E} \times \boldsymbol{B}$ shear flow is at a relatively low level and the large-scale turbulent convection is dominant in the nonlinear saturated state. By increasing the heat flux above a certain threshold, the increased turbulent intensity produces the nonlinear energy transfer from thermal energy to the $\boldsymbol{E} \times \boldsymbol{B}$ kinetic energy, and then from turbulent to mean $\boldsymbol{E} \times \boldsymbol{B}$ flows. Consequently, a transition to the second regime occurs, in which a strong mean $\boldsymbol{E} \times \boldsymbol{B}$ shear flow is generated just inside the LCFS. The mean $\boldsymbol{E} \times \boldsymbol{B}$ shear flow reduces turbulent transport and leads to improved plasma confinement.

II. MODEL EQUATIONS

The simulation model is based on the drift-reduced Braginskii equations [6, 7]. The simplified hot-ion model consists of the ion continuity equation

$$\frac{dn}{dt} + n\nabla \cdot \boldsymbol{v}_E + \nabla \cdot (n\boldsymbol{v}_{di}) + \nabla_{||}(n\boldsymbol{v}_{||i}) = S_n \ , \tag{1}$$

the ion pressure equation

$$\frac{3}{2}\frac{dp_i}{dt} + \frac{5}{2}p_i\nabla \cdot (\boldsymbol{v}_E + \boldsymbol{v}_{||i}) = S_E \ , \tag{2}$$

the vorticity equation $\nabla \cdot \boldsymbol{j} = 0$ for the total current

$$\nabla \cdot \frac{enc}{B\Omega_i}\frac{d}{dt}(-\nabla_\perp\phi - \frac{\nabla_\perp p_i}{en}) + \nabla \cdot \boldsymbol{j}_d + \nabla_{||}j_{||} = 0 \ , \tag{3}$$

where $d/dt = \partial/\partial t + \boldsymbol{v}_E \cdot \nabla$ with $\boldsymbol{v}_E = (c/B)\boldsymbol{b} \times \nabla\phi$, $\Omega_i = eB/m_ic$, $j_{||} = en(\boldsymbol{v}_{||i} - \boldsymbol{v}_{||e})$, and the diamagnetic current $\boldsymbol{j}_d = en\boldsymbol{v}_{di} = (c/B)\boldsymbol{b} \times \nabla p_i$. The plasma compressibility terms $\nabla \cdot \boldsymbol{v}_E = \hat{C}\phi$ and $\nabla \cdot \boldsymbol{j}_d = \hat{C}p_i$ where $\hat{C} = (2c/B)\boldsymbol{b} \times \boldsymbol{\kappa} \cdot \nabla$ denotes the curvature operator due to the magnetic field gradient and field line curvature $\boldsymbol{\kappa} = \boldsymbol{b} \cdot \nabla\boldsymbol{b}$. The term $\nabla_\perp p_i$ in Eq. (3)

represents the contribution of ion diamagnetic drift to the polarization current [3, 4, 6–8], which is the crucial difference from the cold ion model [9–19]. The source terms S_n and S_E are added in Eqs. (1) and (2) to represent the particle and heat fluxes from the inner core region. In our model, the only place we need electron temperature is the sheath boundary conditions applied in the open field line region, where the electron temperature is needed for calculating the sound speed. For simplicity, the electron temperature is set by the ion temperature, which is a simplication to the physics in the SOL region of a tokamak. Since we only use the assumption of equal temperatures for the evaluation of parallel losses, the basic physics of mean $\boldsymbol{E} \times \boldsymbol{B}$ flow generation inside the LCFS shown in this model should be robust.

In the simulation, the coordinate z is aligned to the magnetic field with $\boldsymbol{b} = \boldsymbol{e}_z$, the x is the distance in the radial direction, and the y is perpendicular to both $\boldsymbol{e}_x$ and $\boldsymbol{e}_z$. Here we consider the outer midplane of a tokamak, and thus the y direction is approximately in the poloidal direction with the strong toroidal magnetic field. The field line curvature is taken as $\boldsymbol{\kappa} = -\boldsymbol{e}_x/R$ where R is the major radius. We normalize $p_i/p_{\rm ref} \to p$, $e\phi/T_{\rm ref} \to \phi$, $n/n_{\rm ref} \to n$, $T_e/T_{\rm ref} \to T$ with constant reference values, the parallel length to the connection length $L_{||}$, the perpendicular lengths $x/\rho_s \to x$, $y/\rho_s \to y$, and wave number $k_y\rho_s \to k_y$ with $\rho_s = c_{s0}/\Omega_i$ and $c_{s0} = \sqrt{T_{\rm ref}/m_i}$, the time $t/t_0 \to t$ and frequency $\omega t_0 \to \omega$ with $t_0 = a/c_{s0}$. Here a denotes the length scale for the time normalization and is taken as the minor radius. By integrating Eqs. (1)-(3) along the field lines and applying the sheath boundary conditions, one obtains the normalized 2D model equations for the full density, pressure, and vorticity [13, 14]

$$\frac{dn}{dt} = \hat{C}p - n\hat{C}\phi - \sigma n\sqrt{T} + S_n + D\nabla_\perp^2 n \ , \tag{4}$$

$$\frac{dp}{dt} = -\frac{5}{3}p\hat{C}\phi - \frac{5}{3}\sigma p\sqrt{T} + S_E + \kappa_\perp \nabla_\perp^2 p \ , \tag{5}$$

$$\frac{dw}{dt} = \hat{C}p + \sigma n\sqrt{T}[1 - \exp(3 - \phi/T)] + \mu\nabla_\perp^2 w \ , \tag{6}$$

where $p = nT$, $d/dt = \partial/\partial t + (a/\rho_s)\boldsymbol{v}_E \cdot \nabla$ and the hot-ion vorticity

$$w = \nabla_\perp^2(\phi + p) \tag{7}$$

is normalized in units of Ω_i. The normalized $\boldsymbol{E} \times \boldsymbol{B}$ flow $\boldsymbol{v}_E = \boldsymbol{b} \times \nabla\phi$ in units of c_{s0} has the radial and poloidal components $v_x = -\partial\phi/\partial y$ and $v_y = \partial\phi/\partial x$. The curvature operator $\hat{C} = -2(a/R)\partial/\partial y$ and perpendicular Laplacian $\nabla_\perp^2 = \partial^2/\partial x^2 + \partial^2/\partial y^2$. The divergence of

ion polarization current has been approximated by the convective derivative of the vorticity dw/dt in Eq. (6). In the open field line region, the sheath boundary conditions give rise to the terms multiplied by the parameter $\sigma = a/L_{||}$. The diffusion coefficients D, $\kappa_\perp$, and μ in units of ρ_s^2/t_0 are chosen to be small so that the convection terms are dominant. The source profiles, e.g., $S_E = S_0 \exp(-x^2/x_0^2)$ are localized in a thin layer of the inner boundary region where large diffusion coefficients for the pressure and density are used to diffuse the fluxes out of the source region and also to flatten the gradients and damp the instability in the source region. The model equations are solved by a finite-difference turbulence code with the centered difference in space and predictor-corrector scheme for time stepping. Periodic boundary conditions are assumed in the poloidal y direction, and Dirichlet (fixed value) boundary conditions are imposed at the radial boundaries for the density, pressure, vorticity, and potential. We consider the following parameters for the convection $a/\rho_s = 100$, parallel losses $\sigma = 0.05$, and magnetic curvature $a/R = 0.3$ with the radial and poloidal box sizes $L_x = 75\rho_s$ and $L_y = 200\rho_s$.

Assuming that perturbations $\delta p, \delta\phi \propto \exp(ik_y y - i\omega t)$ with $k_{||} = 0$ and linearizing Eqs. (5)-(6) in the absence of dissipation and background $\boldsymbol{E} \times \boldsymbol{B}$ shear flows, one obtains the interchange mode with the normalized dispersion relation $\omega^2 - (\omega + \omega_d/k_y^2)(\omega_{*i} + 5\omega_d/3) = 0$, where the curvature frequency $\omega_d = 2k_y a/R$, the ion diamagnetic frequency $\omega_{*i} = -k_y a/L_p$ and the pressure gradient scale length $L_p = -p_0/(dp_0/dx)$. For $\omega = \omega_r + i\gamma$ in units of c_{s0}/a, the real frequency $\omega_r = (\omega_{*i} + 5\omega_d/3)/2 = -k_y(a/R)(R/L_p - 10/3)/2$ and the growth rate

$$\gamma = \frac{a}{R}\sqrt{2(R/L_p - 10/3) - k_y^2(R/L_p - 10/3)^2/4}\ . \tag{8}$$

For pressure gradients steeper than a critical gradient, the interchange mode becomes unstable in the bad curvature region and the perturbations propagate in the ion diamagnetic drift direction. The plasma compressibility term $\nabla \cdot \boldsymbol{v}_E$ in Eq. (2) leads to the critical pressure gradient ($R/L_p = 10/3$) for the marginal stability. The ion diamagnetic term $\nabla_\perp^2 \delta p$ in Eq. (7) gives rise to the non-zero real frequency ω_r and the stabilizing contribution of the k_y^2 term in the growth rate, which makes the high k_y modes less unstable.

Taking poloidal averages of Eq. (6) in the absence of dissipation and decomposing the full quantities into the mean and fluctuating parts (e.g., $w = w_0 + \delta w$), one obtains the evolution equation for the mean vorticity

$$\frac{\partial w_0}{\partial t} = -(a/\rho_s)\frac{d}{dx}\left\langle \delta w \delta v_x \right\rangle\ , \tag{9}$$

where $\langle\cdots\rangle = \int_0^{L_y} dy/L_y$ denotes the poloidal averages and the mean vorticity $w_0 = \langle w\rangle$. Thus the formation of negative gradients in the radial vorticity flux $\langle\delta w\delta v_x\rangle$ increases the mean vorticity $w_0 = \nabla_\perp^2(\phi_0 + p_0)$. Note that $\nabla_\perp^2\delta p \gg \nabla_\perp^2 p_0$ due to the scale separation of perturbations and background profiles in the nonlinear phase. Thus the vorticity $w \simeq \nabla_\perp^2(\phi+\delta p)$ and the mean vorticity $w_0 \simeq \nabla_\perp^2\phi_0$ is dominated by the mean $\boldsymbol{E}\times\boldsymbol{B}$ flow shear.

The transfer of thermal energy to the $\boldsymbol{E}\times\boldsymbol{B}$ kinetic energy can be shown from Eqs. (5) and (6) in the absence of energy source and dissipation [6, 10, 11]. Integrating Eq. (5) over all space, one obtains the evolution of thermal energy $(3/2)\int(\partial p_0/\partial t)dx/L_x = -F_p$, where the transfer power

$$F_p = \int \frac{dx}{L_x}\left\langle p\hat{C}\phi\right\rangle = 2(a/R)\int\frac{dx}{L_x}\langle\delta p\delta v_x\rangle \tag{10}$$

is related to the volume-averaged turbulent energy flux $\langle\delta p\delta v_x\rangle$. Multiplying Eq. (6) by ϕ and integrating over all space, one obtains the evolution of the fluid kinetic energy

$$\int\frac{dx}{L_x}\left\langle\frac{1}{2}\frac{\partial}{\partial t}|\nabla_\perp\phi|^2 + \nabla_\perp\phi\cdot\frac{\partial}{\partial t}\nabla_\perp p\right\rangle = F_p\ . \tag{11}$$

Thus a positive transfer power F_p converts thermal energy to the $\boldsymbol{E}\times\boldsymbol{B}$ kinetic energy.

Next we review the energy transfer between the turbulent and mean $\boldsymbol{E}\times\boldsymbol{B}$ flows for the cold ion case. Multiplying Eq. (9) by ϕ_0 and integrating over all space, one obtains the evolution of mean $\boldsymbol{E}\times\boldsymbol{B}$ flow energy [11]

$$\frac{1}{2}\frac{\partial U}{\partial t} = (a/\rho_s)\int\frac{dx}{L_x}(-\frac{d\phi_0}{dx})\frac{d}{dx}\langle\delta v_x\delta v_y\rangle = F_v\ , \tag{12}$$

where $U = \int|\nabla_\perp\phi_0|^2dx/L_x$ indicates the volume-averaged kinetic energy of mean $\boldsymbol{E}\times\boldsymbol{B}$ flow, the Reynolds stress $\langle\delta v_x\delta v_y\rangle$ represents the correlation of $\boldsymbol{E}\times\boldsymbol{B}$ velocity fluctuations, and F_v denotes the volume-averaged Reynolds power, which is essentially a product of mean potential gradient and the Reynolds force $d\langle\delta v_x\delta v_y\rangle/dx$. Subtraction of Eq. (9) from Eq. (6) yields the equation for the fluctuating vorticity δw. Multiplying the resulting equation by $\delta\phi$ and integrating over all space, one obtains the evolution of turbulent $\boldsymbol{E}\times\boldsymbol{B}$ flow energy [11]

$$\frac{1}{2}\frac{\partial K}{\partial t} = F_p - F_v\ , \tag{13}$$

where $K = \int\langle|\nabla_\perp\delta\phi|^2\rangle\,dx/L_x$ indicates the volume-averaged turbulent $\boldsymbol{E}\times\boldsymbol{B}$ kinetic energy. Thus a positive transfer power F_p acts as the energy source for turbulent $\boldsymbol{E}\times\boldsymbol{B}$ flows, and a positive Reynolds power F_v indicates the energy transfer from turbulent to mean $\boldsymbol{E}\times\boldsymbol{B}$ flows and acts as the energy sink for the fluctuation.

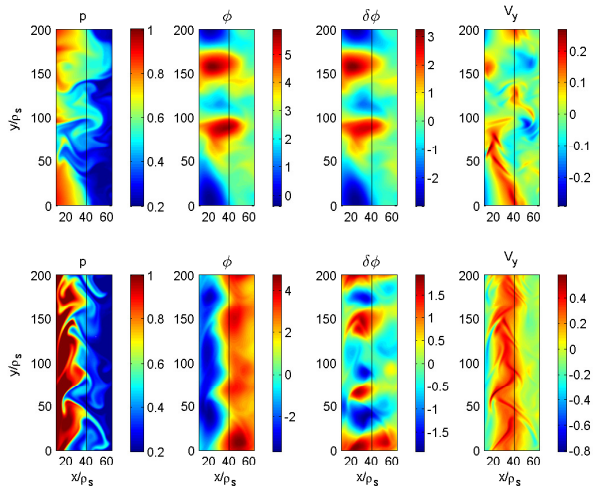

FIG. 1. Typical structures of the full pressure p, full potential ϕ, fluctuating potential $\delta\phi$, and the poloidal $\boldsymbol{E} \times \boldsymbol{B}$ flow v_y in the first (top) and second (bottom) regimes. The location of the LCFS is at $x = 40$ as indicated by the vertical black line.

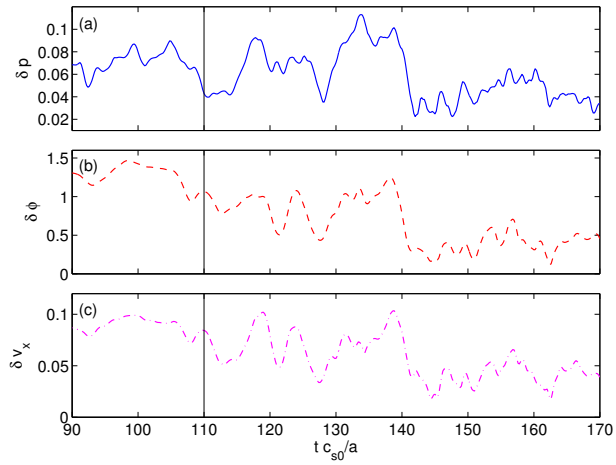

FIG. 2. Typical evolution of fluctuation amplitude (standard deviation) of (a) pressure $\sqrt{\langle \delta p^2 \rangle}$, (b) potential $\sqrt{\langle \delta \phi^2 \rangle}$, (c) radial $\boldsymbol{E} \times \boldsymbol{B}$ velocity $\sqrt{\langle \delta v_x^2 \rangle}$. The vertical line indicates the time with increased heating.

III. SIMULATION RESULTS

The simulations are started with small-amplitude perturbations and the interchange instability is then triggered by initially steep pressure gradients. In the linear phase, the perturbations grow exponentially and develop small-scale eddies with $k_y L_p \sim 1$ in the pressure gradient region. In the simulation, the long wavelength ideal modes with $k_y L_p \ll 1$

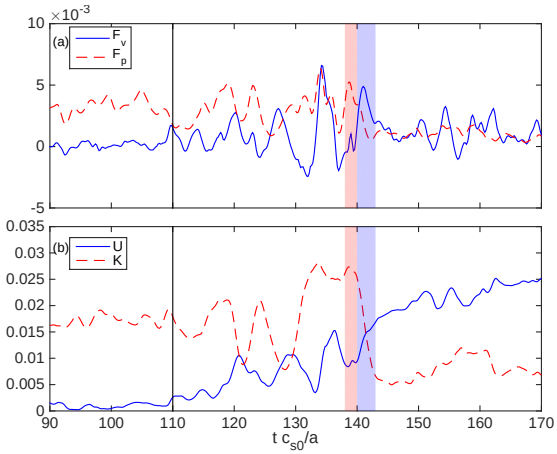

FIG. 3. Typical evolution of the volume-averaged (a) transfer power F_p and F_v, (b) turbulent and mean $\boldsymbol{E} \times \boldsymbol{B}$ flow energy K and U. Black vertical line indicates the time with increased heating. Red and blue time windows indicate just before and during the transition.

are stable because of the radial localization of the pressure gradient, and shorter wavelength modes with $k_y L_p \gg 1$ are stabilized by a combination of ion diamagnetic effects shown in Eq. (8) and the $\boldsymbol{E} \times \boldsymbol{B}$ flow shear [3]. The radial mixing of plasma by the $\boldsymbol{E} \times \boldsymbol{B}$ eddies flattens the background pressure gradients so that long wavelength modes begin to grow in the early nonlinear phase. The wave number spectra of the pressure and potential become broad and the spectral peak is down-shifted to the lower k_y (long wavelengths) modes in the nonlinear phase. The relaxation of pressure gradients to the critical gradient ultimately leads to the nonlinear saturation of unstable modes.

Eventually, a steady state of the first regime is reached, in which the radial convective transport and parallel losses are in balance. As shown in Fig. 1, the large-scale turbulent $\boldsymbol{E} \times \boldsymbol{B}$ eddies are developed in the nonlinear saturated state and the potential structures are dominated by the fluctuating potential $\delta\phi$. The radially broad eddies near the LCFS produce intermittent, convective transport of plasma from closed to open field line regions, where the parallel losses give rise to the dissipation. Figure 2 shows the large-amplitude fluctuations of pressure, potential, and radial $\boldsymbol{E} \times \boldsymbol{B}$ velocity: $\delta p/p_0 \sim 0.1$, $\delta\phi/\phi_0 \sim 1/3$, $\delta v_x/c_{s0} \sim 0.1$. As seen in Fig. 3, the amplitudes of turbulent and mean $\boldsymbol{E} \times \boldsymbol{B}$ flows are changed in time under the influence of the transfer power F_p and Reynolds power F_v. Note that the transfer power F_p is positive and much larger than the Reynolds power F_v which fluctuates around zero. As a result, the mean flow energy is at a low level and the $\boldsymbol{E} \times \boldsymbol{B}$

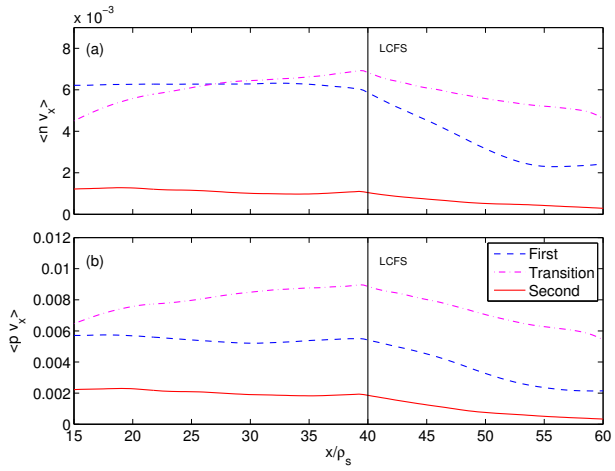

FIG. 4. Typical time-averaged profile of radial turbulent fluxes of particle $\langle \delta n \delta v_x \rangle$ and energy $\langle \delta p \delta v_x \rangle$ in the first and second regimes, and just before transition.

kinetic energy is dominated by the turbulent flows. The positive energy and particle fluxes in Fig. 4 indicate the radially outward convective transport, and the turbulent fluxes are almost constant inside the LCFS for a long time average and decreases outside the LCFS due to the parallel losses. The time-averaged vorticity flux and Reynolds stress in Fig. 5 are flat and small. The profile gradients of pressure, density and potential are flat with small mean $\boldsymbol{E} \times \boldsymbol{B}$ shear flow, as seen in Figs. 6 and 7. The system is near the marginal stability with the pressure profile gradients set by the critical gradient. Note that the boundary layers such as the source region have been excluded from the results presented and the profiles have been averaged over time and the poloidal y direction.

Starting from the steady state of the first regime, we next only increase the heat flux that drives the system by raising the heating power S_E and the pressure value at the inner boundary, while keeping the other parameters the same. As seen in Fig. 2, the large-amplitude pressure fluctuation is induced with the increased heat flux, which produces large-amplitude fluctuations of potential and $\boldsymbol{E} \times \boldsymbol{B}$ velocity due to the coupling of $\nabla_\perp^2 \delta\phi$ and $\nabla_\perp^2 \delta p$ in Eq. (7). As a result, the large-amplitude oscillations of transfer power F_p and F_v are also induced, which give rise to the large-amplitude oscillations of turbulent and mean $\boldsymbol{E} \times \boldsymbol{B}$ flow energy, as seen in Fig. 3. In particular, the turbulent $\boldsymbol{E} \times \boldsymbol{B}$ kinetic energy K increases with the positive transfer power F_p, which converts thermal energy to turbulent flows. Following the rise of fluctuations, the mean $\boldsymbol{E} \times \boldsymbol{B}$ flow energy U grows as the positive Reynolds power F_v increases. After some time period of oscillations, the large-amplitude

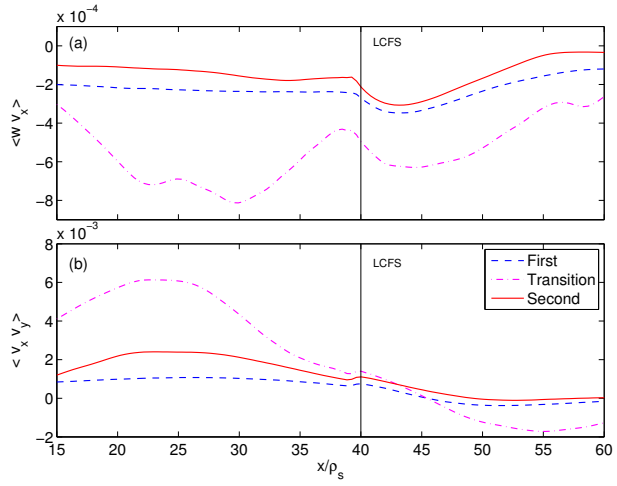

FIG. 5. Typical time-averaged profile of (a) vorticity flux $\langle \delta w \delta v_x \rangle$, (b) Reynolds stress $\langle \delta v_x \delta v_y \rangle$ in the first and second regimes, and during the transition.

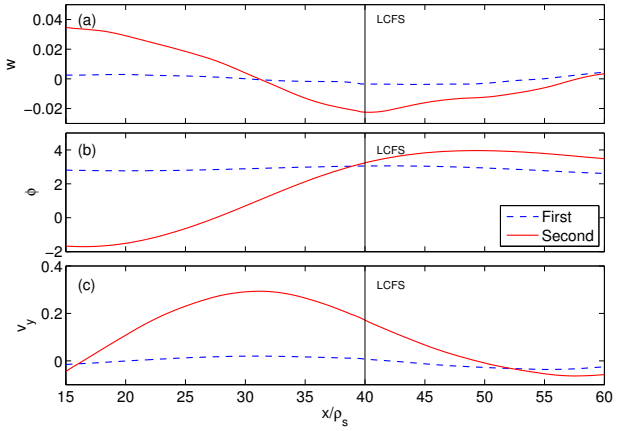

FIG. 6. Typical time-averaged profile of (a) vorticity w_0, (b) potential ϕ_0, (c) poloidal $\boldsymbol{E} \times \boldsymbol{B}$ flow v_{y0} in the first and second regimes.

positive Reynolds power ($F_v > 0$) is eventually induced when the heat flux that drives the system is above a certain threshold. During the time period of transition (blue time window $t = 140 - 143$ in Fig. 3), the time-averaged positive Reynolds power becomes larger than the transfer power (i.e., $F_v > F_p$), which suggests a definite transfer of energy from turbulent to mean $\boldsymbol{E} \times \boldsymbol{B}$ flows. As a result, the mean $\boldsymbol{E} \times \boldsymbol{B}$ flow energy increases to a much higher level, and the turbulent $\boldsymbol{E} \times \boldsymbol{B}$ flow energy decreases significantly. After the transition, the fluctuation levels of pressure and potential are reduced so that the amplitudes of transfer power F_p and F_v also decrease.

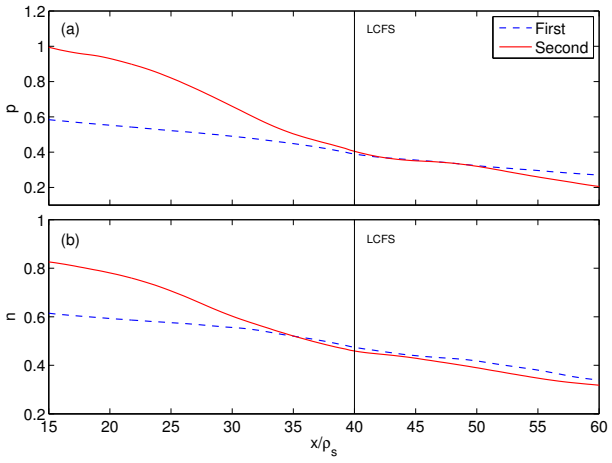

FIG. 7. Typical time-averaged profile of (a) pressure p_0 and (b) density n_0 in the first and second regimes.

In the simulation, the changes in heating power over the time range of interest are as follows: $S_E = 0.02$ in the first regime, $S_E = 0.2$ at the transition, and $S_E = 0.1$ in the second regime. Note that the value of heating power in the second regime is much higher than that in the first regime, while the fluctuations in the second regime are lower than those in the first regime due to the generation of mean $\boldsymbol{E} \times \boldsymbol{B}$ shear flow during the transition. The heating power is reduced after the transition (from $S_E = 0.2$ to 0.1) so that the growth of mean $\boldsymbol{E} \times \boldsymbol{B}$ flow saturates and a steady state is reached in the second regime.

Next we examine the changes in the spatial structures with increased heating. For the short time period just before transition (red time window $t = 138 - 140$ in Fig. 3), the fluctuation amplitudes increase to a high level as shown in Fig. 2. The stronger turbulence intensity increases the turbulent energy fluxes across the LCFS, as shown in Fig. 4. Since the pressure gradients near the LCFS drive the turbulence in the system, the turbulent fluxes tend to peak at the LCFS where the turbulence is strongest.

During the time period of transition, the radial vorticity flux in Fig. 5(a) becomes more negative with increased amplitude and forms the negative gradients inside the LCFS. As shown in Eq. (9), this produces the increased positive mean vorticity $w_0 \simeq \nabla_\perp^2 \phi_0$. On the other hand, the plasma potential in the open field line region decreases with the electron temperature $\phi_0 \simeq 3T_0$ due to the sheath boundary conditions. Thus the potential profile drops just inside the LCFS, producing stronger mean potential gradients. During the transition, the Reynolds stress in Fig. 5(b) also increases and forms the negative gradient inside

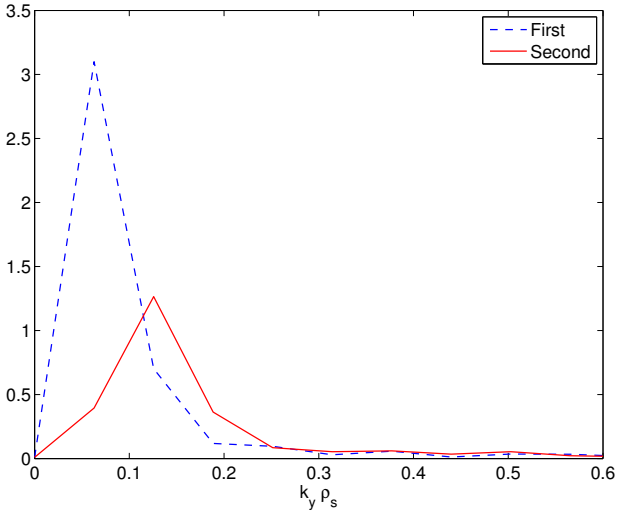

FIG. 8. Typical wave number spectrum of the fluctuating potential $|\delta\phi(k_y)|$ in the first and second regimes.

the LCFS. This implies the increased Reynolds force and more negative vorticity flux, since the $\boldsymbol{E}\times\boldsymbol{B}$ vorticity flux $\langle\delta v_x\nabla_\perp^2\delta\phi\rangle = d\langle\delta v_x\delta v_y\rangle/dx$. Combined with the positive mean potential gradients inside the LCFS, this leads to the increased positive Reynolds power as shown in Eq. (12).

After the transition, the potential structures are dominated by the mean potential ϕ_0. As seen in Figs. 1 and 6, the potential well structure generates a strong mean $\boldsymbol{E}\times\boldsymbol{B}$ shear flow $v_{y0} = d\phi_0/dx$ in the poloidal direction, which corresponds to a negative well structure of mean radial electric field E_r just inside the LCFS. The mean $\boldsymbol{E}\times\boldsymbol{B}$ shear flow reduces the amplitude and radial correlation lengths of turbulent eddies so that the wave number spectral peak of the fluctuating potential in Fig. 8 is up-shifted to higher k_y modes with lower amplitude. This causes the reduction of radial turbulent transport across the radial domain, as seen in Fig. 4. Consequently, the pressure and density profiles in Fig. 7 form steep gradients just inside the LCFS, which indicates improved energy and particle confinement. Note that the steepening of mean pressure gradient occurs in a small region where the mean potential gradient is largest. As shown in Fig. 5, the amplitudes of Reynolds stress and vorticity flux are reduced due to the lower level of fluctuations in the second regime.

To examine how the turbulent and mean ion diamagnetic flows compete with the $\boldsymbol{E}\times\boldsymbol{B}$ flows, we compare the amplitude of poloidal $\boldsymbol{E}\times\boldsymbol{B}$ flow $v_{Ey} = \partial\phi/\partial x$ and ion diamagnetic flow $v_{diy} = \partial p/\partial x$ normalized in units of c_{s0}. Figure 9 shows that the $\boldsymbol{E}\times\boldsymbol{B}$ flows are much

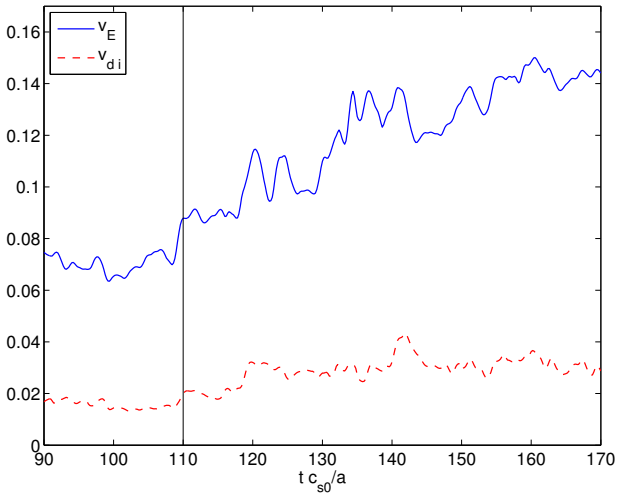

FIG. 9. Typical evolution of the amplitude of poloidal $\boldsymbol{E}\times\boldsymbol{B}$ flow v_{Ey} and ion diamagnetic flow v_{diy}. The vertical line indicates the time with increased heating.

larger than the ion diamagnetic flows in the first regime and during the transition. Thus the growth of mean $\boldsymbol{E}\times\boldsymbol{B}$ flow during the transition is due to the nonlinear energy transfer induced by enhanced fluctuations.

Finally, we consider a hot-ion model with constant density, in which only the pressure and vorticity equations (5)-(7) are evolved. The simulations show that a similar transition from the low to high confinement regimes is reproduced by increasing the heat flux above a certain threshold. Consistent with Ref. [3], we find that the ion diamagnetic term $\nabla_\perp^2\delta p$ in the vorticity is required to produce a transition. Without the ion diamagnetic term (i.e., the cold ion model), the simulations show that the Reynolds power always fluctuates around zero and thus the mean $\boldsymbol{E}\times\boldsymbol{B}$ flow stays at a low level without a transition.

IV. CONCLUSION

In summary, the fluctuation-induced $\boldsymbol{E}\times\boldsymbol{B}$ shear flow and energy transfer in the interchange turbulence have been explored in a flux-driven system with both closed and open field line regions. The transfer of energy between fluctuations and sheared flows in two confinement regimes is presented, with implications for the evolution of the Reynolds stress, radial fluxes of energy and vorticity, and ultimately the plasma profiles of pressure, density, and potential. By increasing the heat flux above a certain threshold, the increased turbulent

intensity gives rise to the nonlinear transfer of energy from fluctuations to mean $\boldsymbol{E}\times\boldsymbol{B}$ flows. As a result, a transition to the second regime occurs, in which a strong mean $\boldsymbol{E}\times\boldsymbol{B}$ shear flow is generated just inside the LCFS. The mean $\boldsymbol{E}\times\boldsymbol{B}$ shear flow reduces the radial turbulent transport, which results in the steepening of pressure gradients and improved energy confinement.

V. ACKNOWLEDGMENTS

We thank B. N. Rogers, R. Waltz, P. Diamond, Z. Lin, X. Q. Xu, H. Qin, K. Gentle, T. Zhou, G. Wang, P. Ricci, O. E. Garcia, B. LaBombard, G. S. Xu, M. Xu, J. Cheng for helpful discussions, and X. Liao, H. Zhang, D. Liu for help with simulations. We also thank the referees for helpful comments. This work was supported by the ITER-China Grant No. 2013GB112006, the NSFC Grant No. J1103206 and the U.S. DOE Contract No. DE-FC02-08ER54966.

[1] P. H. Diamond, S.-I. Itoh, K. Itoh, and T. S. Hahm, Plasma Phys. Control. Fusion **47**, R35 (2005).

[2] Z. Yan, G. McKee, R. J. Fonck, P. Gohil, R. J. Groebner, and T. Osborne, Phys. Rev. Lett. **112**, 125002 (2014).

[3] B. N. Rogers, J. F. Drake, and A. Zeiler, Phys. Rev. Lett. **81**, 4396 (1998).

[4] X. Q. Xu, R. H. Cohen, T. D. Rognlien, and J. R. Myra, Phys. Plasmas **7**, 1951 (2000).

[5] X. Q. Xu, W. M. Nevins, R. H. Cohen, J. R. Myra, and P. B. Snyder, New Journal of Physics **4**, 53.1 (2002).

[6] A. Zeiler, J. F. Drake, and B. Rogers, Phys. Plasmas **4**, 2134 (1997).

[7] A. N. Simakov and P. J. Catto, Phys. Plasmas **10**, 4744 (2003).

[8] B. Scott, Plasma Phys. Control. Fusion **40**, 823 (1998).

[9] J. R. Myra, D. A. Russell, and D. A. D'Ippolito, Phys. Plasmas **15**, 032304 (2008).

[10] O. E. Garcia, V. Naulin, A. Nielsen, and J. Rasmussen, Phys. Rev. Lett. **92**, 165003 (2004).

[11] O. E. Garcia, N. H. Bian, J.-V. Paulsen, S. Benkadda, and K. Rypdal, Plasma Phy. Control. Fusion **45**, 919 (2003).

[12] O. E. Garcia, V. Naulin, A. H. Nielsen, and J. J. Rasmussen, Phys. Plasmas **12**, 062309 (2005).

[13] P. Ricci, B. N. Rogers, and S. Brunner, Phys. Rev. Lett. **100**, 225002 (2008).

[14] B. Li, B. N. Rogers, P. Ricci, and K. W. Gentle, Phys. Plasmas **16**, 082510 (2009).

[15] P. Ricci and B. N. Rogers, Phys. Rev. Lett. **104**, 145001 (2010).

[16] B. Li, B. N. Rogers, P. Ricci, K. W. Gentle, and A. Bhattacharjee, Phys. Rev. E **83**, 056406 (2011).

[17] L. Chôné, P. Beyer, Y. Sarazin, G. Fuhr, C. Bourdelle, and S. Benkadda, Phys. Plasmas **21**, 070702 (2014).

[18] L. Chôné, P. Beyer, Y. Sarazin, G. Fuhr, C. Bourdelle, and S. Benkadda, Nucl. Fusion **55**, 073010 (2015).

[19] G. Y. Park, S. S. Kim, H. Jhang, P. H. Diamond, T. Rhee, and X. Q. Xu, Phys. Plasmas **22**, 032505 (2015).

[20] I. Cziegler, G. R. Tynan, P. H. Diamond, A. E. Hubbard, J. W. Hughes, J. Irby, and J. L. Terry, Plasma Phys. Control. Fusion **56**, 075013 (2014).

[21] G. S. Xu, H. Q. Wang, M. Xu, B. N. Wan, H. Y. Guo, P. H. Diamond, G. R. Tynan, R. Chen, N. Yan, D. F. Kong, H. L. Zhao, A. D. Liu, L. Lan, V. Naulin, A. H. Nielsen, J. J. Rasmussen, K. Miki, P. Manz, W. Zhang, L. Wang, L. M. Shao, S. C. Liu, L. Chen, S. Y. Ding, N. Zhao, Y. L. Li, Y. L. Liu, G. H. Hu, X. Q. Wu, and X. Z. Gong, Nucl. Fusion **54**, 103002 (2014).

[22] M. A. Malkov, P. H. Diamond, K. Miki, J. E. Rice, and G. R. Tynan, Phys. Plasmas **22**, 032506 (2015).

[23] L. Schmitz, L. Zeng, T. L. Rhodes, J. C. Hillesheim, W. A. Peebles, R. J. Groebner, K. H. Burrell, G. R. McKee, Z. Yan, G. R. Tynan, P. H. Diamond, J. A. Boedo, E. J. Doyle, B. A. Grierson, C. Chrystal, M. E. Austin, W. M. Solomon, and G. Wang, Nucl. Fusion **54**, 073012 (2014).

[24] M. Xu, G. R. Tynan, P. H. Diamond, P. Manz, C. Holland, N. Fedorczak, S. C. Thakur, J. H. Yu, K. J. Zhao, J. Q. Dong, J. Cheng, W. Y. Hong, L. W. Yan, Q. W. Yang, X. M. Song, Y. Huang, L. Z. Cai, W. L. Zhong, Z. B. Shi, X. T. Ding, X. R. Duan, Y. Liu, and HL-2A Team, Phys. Rev. Lett. **108**, 245001 (2012).

[25] J. Cheng, J. Q. Dong, K. Itoh, L. W. Yan, M. Xu, K. J. Zhao, W. Y. Hong, Z. H. Huang, X. Q. Ji, W. L. Zhong, D. L. Yu, S.-I. Itoh, L. Nie, D. F. Kong, T. Lan, A. Liu, X. L. Zou,

Q. W. Yang, X. T. Ding, X. R. Duan, Y. Liu, and HL-2A Team, Phys. Rev. Lett. **110**, 265002 (2013).